RSC Advances

PAPER

View Article Online
View Journal | View Issue

Cite this: *RSC Adv.*, 2018, **8**, 4284

Fabrication of magnetically separable $NiFe_2O_4$/BiOI nanocomposites with enhanced photocatalytic performance under visible-light irradiation

Yongmei Xia,[a] Zuming He, *[b] Jiangbin Su,[c] Bin Tang,[c] Kejun Hu,[a] Yaling Lu,[a] Shunping Sun[a] and Xiaoping Li[a]

A series of novel flower-like $NiFe_2O_4$/BiOI (NFO/BOI) nanocomposites have been synthesized *via* a facile solvothermal method. The structure, morphology and magnetic, optical and visible-light photocatalytic properties of the as-prepared nanocomposite were respectively characterized by X-ray diffraction, field-emission scanning electron microscopy, energy dispersive X-ray spectroscopy, transmission electron microscopy, X-ray photoelectron spectroscopy, photoluminescence spectroscopy, vibrating sample magnetometry and UV-visible diffuse reflectance spectroscopy. Experimental results revealed that the weight percent of $NiFe_2O_4$ has a considerable effect on the photodegradation of rhodamine B, methylene blue and crystal violet under visible-light irradiation. Compared with pure $NiFe_2O_4$ and BiOI, all the heterogeneous NFO/BOI nanocomposites exhibited significantly enhanced photocatalytic efficiency. Among these prepared samples, the $NiFe_2O_4$/BiOI nanocomposite with 15% wt $NiFe_2O_4$ displayed the best photocatalytic activity. The enhanced photocatalytic performance was mainly ascribed to the efficient separation of photo-induced electron–hole pairs and the formation of highly active species, superoxide radicals ($^{\bullet}O_2^{-}$), in the NFO/BOI photocatalytic oxidation system. Furthermore, the NFO/BOI nanocomposites could be easily separated and recycled from contaminant solution using a magnet, which exhibited great potential application in the treatment of various pollutants in wastewater by utilizing solar energy effectively.

Received 18th November 2017
Accepted 15th January 2018

DOI: 10.1039/c7ra12546a

rsc.li/rsc-advances

1. Introduction

With the development of the world economy and the acceleration of social activities, human consumption of energy has been increasing. More and more harmful dye pollutants have been released into the environment. The energy and environmental problems are increasingly prominent, which have become two major issues urgently needing to be solved.[1–3] Solar energy is the cleanest and safest source of energy among all kinds of energy sources. Therefore, research on photocatalysis technology using the solar energy degradation of organic pollutants has been become one of the hottest research topics with regard to energy and environment.[4–6] The main advantage of this photocatalytic degradation technology is complete degradation of organic pollutants to CO_2, H_2O and other inorganic constituents with solar energy as an endless energy source,[7–10] using catalysts such as TiO_2 (ref. 11 and 12) and ZnO.[13,14] However, these catalysts only absorb 4% of the solar spectrum energy due to their wide band gap.[15] In the last decade, Bi-based compounds like BiOX (X = Cl, Br and I) have attracted much attention because of their unique tetragonal matlockite structures.[16–18] In the bismuth oxyhalides, the band gap of BiOI is the narrowest [E_g = 1.7–1.9] with its absorption band edge extending to 680 nm and light absorption range covering almost all the visible light range (390–760 nm). Therefore, BiOI has a good visible-light response and may be a promising photocatalyst. Unfortunately, as a photocatalyst, pure BiOI has some shortcomings such as facile electron–hole pairs recombination under visible-light irradiation, difficult separation and recycling from wastewater, and easy secondary pollution, which would greatly limit its practical application. To improve its photocatalytic activity, some effort has been made to find other efficient semiconductors to form BiOI-based composites such as Fe_3O_4/BiOI[19] and BiOI/TiO_2 (ref. 20) to enhance the charge separation. These composites were demonstrated to show higher photocatalytic properties.

$NiFe_2O_4$ is a narrow band gap semiconductor material, which has magnetic separability, chemical stability and photocatalytic property.[21–23] It thus has wide applications in the field of catalysis, magnetic devices, lithium ion batteries and water treatment[24–27] and has attracted much attention of researchers. In particular, due to its photocatalytic activity and easy recovery

[a]Jiangsu Key Laboratory of Advanced Material Design and Additive Manufacturing, School of Materials and Engineering, Jiangsu University of Technology, Changzhou 213001, China

[b]Huaide College, Changzhou University, Jingjiang 214500, China. E-mail: hzm432928@cczu.edu.cn

[c]School of Mathematics and Physics, Changzhou University, Changzhou 213164, China

of magnetic properties, $NiFe_2O_4$ has a broad application prospect in sewage treatment. Unsatisfactorily, under visible-light irradiation, pure $NiFe_2O_4$ exhibits lower photocatalytic activity because of a fast recombination of photoelectron–hole pairs. Considering their own characteristics of the BiOI and $NiFe_2O_4$, once $NiFe_2O_4$ is introduced to BiOI, they may overcome the above defects. To our best knowledge, preparation of magnetically separable photocatalyst through coupling BiOI to $NiFe_2O_4$ has not been reported yet. Hence, we expect that it is meaningful to attempt to add $NiFe_2O_4$ to BiOI photocatalyst and there is a wide range of application of the $NiFe_2O_4$/BiOI (NFO/BOI) nanocomposites.

In this paper, we successfully prepared magnetically separable NFO/BOI nanocomposites by a facile two-step route. Then the photocatalytic performance of as-synthesized NFO/BOI nanocomposites was investigated by degradation three kinds of dyes under visible-light irradiation. Finally, the possible photocatalytic mechanism was also proposed.

2. Experimental

2.1. Materials

Bismuth nitrate ($Bi(NO_3)_3 \cdot 5H_2O$), iron chloride hexahydrate ($FeCl_3 \cdot 6H_2O$), sodium hydroxide (NaOH), ethylene glycol ($C_2H_6O_2$), nickel chloride hexahydrate ($NiCl_2 \cdot 6H_2O$) and potassium iodide (KI) were purchased from Aladdin Industrial Co., Ltd (Shanghai, China). All the reagents were of analytical grade and used without any further purification.

2.2. Preparation of NFO/BOI nanocomposites

The NFO/BOI nanocomposites were synthesized by a two-step method, combining $NiFe_2O_4$ and BiOI fabrication by solvothermal method route. The specific preparation process is as follows:

2.2.1 Preparation of $NiFe_2O_4$. The first step, 0.1 mol $FeCl_3 \cdot 6H_2O$ was dissolved into 150 mL distilled water under stirring. The second step, 0.05 mol $NiCl_2 \cdot 6H_2O$ was dissolved into the $FeCl_3$ aqueous solution of $FeCl_3$ under dramatic magnetic stirring for 20 min. The pH of this solution was then adjusted to 12.0 with NaOH solution, and the red-brown product gradually precipitated from the solution. The last step, the red-brown products was collected, repeatedly washed with distilled water, and then annealed at 500 °C for 3 h in air, the reddish brown $NiFe_2O_4$ powder was obtained.

2.2.2 Preparation of the NFO/BOI nanocomposites. The first step, 4.851 g of $Bi(NO_3)_3 \cdot 5H_2O$ was dissolved in 50 mL of ethylene glycol under magnetic stirring for 20 min, which was drop-wisely added into the same volume of (1.66 g) KI dissolved in ethylene glycol under magnetic stirring for 20 min. The second step, 0.4 g $NiFe_2O_4$ were added to the above mixed solution and stirred at room temperature for 1 h. Then the mixture solution by transferred to a Teflon-lined autoclave at 140 °C for 36 h. The autoclave was naturally cooled to room temperature. The last step, the solid products was washed by deionized water and then dried at 80 °C to obtain 10 wt% $NiFe_2O_4$/BiOI (10-NFO/BOI) nanocomposites. Other 5-NFO/BOI, 15-NFO/BOI, 20-NFO/BOI nanocomposites materials with different $NiFe_2O_4$ content were fabricated by the same method.

2.3. Structure characterization

The phases and crystalline structure were studied by X-ray diffraction (XRD) with Cu Kα (λ = 0.15418 nm) radiation (D/max-2500, Rigaku) of synthesized catalysts. Morphologies and particle sizes were investigated using a field-emission scanning electron microscope (FE-SEM, SUAPR55, Germany Zeiss) with energy-disperse X-ray spectroscopy (EDS). Valence states of element were detected by X-ray Photoelectron Spectroscopy of synthesized catalysts (XPS, ESCALAB 250Xi, Thermo Fisher Scientific, USA). The transmission electron microscopy (TEM) analysis was performed in a JEOL JEM-200CX microscope, operating at 200 kV. The UV-vis diffuse reflectance spectra (DRS) were obtained using a UV-vis spectrophotometer (UV-2450, Shimadzu). The photoluminescence (PL) spectra were measured using a fluorescence spectrophotometer of the samples (FLs980, Edinburgh, UK). The magnetic measurement was conducted with vibrating sample magnetometer (VSM). Electrochemical measurement was conducted with electrochemical analyzer (CHI660C Instruments, Shanghai, China) in a conventional three electrode cell, using an Ag/AgCl electrode (3 M KCl) as the reference electrode and a Pt plate as the counter electrode.

2.4. Photocatalytic evaluation studies

The performance of photocatalysis of as-fabricated samples was evaluated by removing rhodamine B (RhB), crystal violet (CV) and methylene blue (MB) under visible-light irradiation. A 500 W xenon lamp equipped with UV cut-off filters (λ > 420 nm) was used as a visible light source, and a light intensity of 0.4 mW cm^{-2} was ensured. 100 mg of as-prepared sample was put into 100 mL (20 mg L^{-1}) dye solution. Prior to irradiation, the dye solution was stirred for 30 min in the dark. During each photocatalytic experiment, 3 mL of the dye solution was withdrawn every 20 minutes and magnetically separated remove catalyst for analysis. The concentration of the dye solution was measured by UV-vis spectroscopy at its maximum absorption.

3. Results and discussion

3.1. XRD analysis

The XRD patterns of as-synthesized samples are presented in Fig. 1. The (111), (220), (311), (222), (400), (422), (511), (400) and (533) crystal planes of spinel $NiFe_2O_4$ (JCPD no. 54-0964) can be indexed to the diffraction peaks at the 2θ values of 18.39°, 30.28°, 35.68°, 37.33°, 43.32°, 53.83°, 57.26°, 62.90° and 74.64°, respectively.[28] Besides, no other impurity peak is found. The exhibited diffraction peaks at 19.36°, 24.29°, 31.65°, 33.16°, 37.05°, 39.36°, 43.64°, 45.37°, 51.34°, 55.15°, 59.18°, 60.20°, 66.12°, 70.04°, 74.09° and 75.13° are conforming to the (002), (101), (110), (111), (103), (004), (113), (200), (114), (212), (213), (115), (220), (116), (302) and (310) crystal planes of BiOI (JCPD No. 10-0445), respectively. The XRD pattern of the 15-NFO/BOI nanocomposites displayed that all the peaks can be well

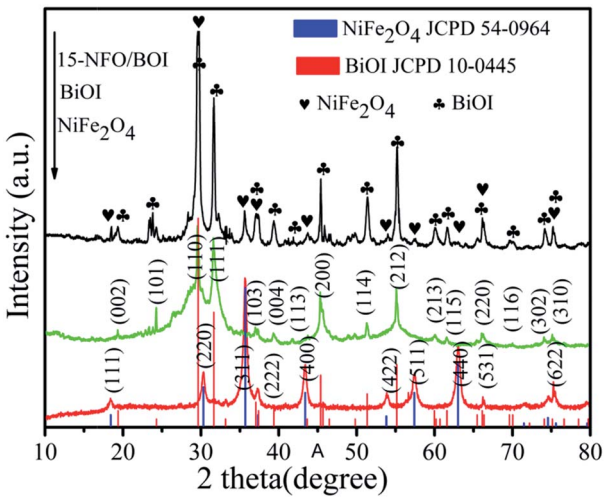

Fig. 1 XRD patterns of BiOI, $NiFe_2O_4$ and 15-NFO/BOI nanocomposites.

indexed to spinel structure of $NiFe_2O_4$ and tetragonal phase of BiOI. There is no obvious peaks of impurity observed, indicating that the NFO/BOI nanocomposites were indeed two-phase hybrids.

3.2. XPS analysis

To investigate the elemental composition and chemical states of the as-prepared samples, XPS measurement was carried out to characterize the 15-NFO/BOI nanocomposites, and the results are displayed in Fig. 2. The XPS survey scan spectrum of $NiFe_2O_4$/BiOI nanocomposites is shown in Fig. 2a, which revealed the existence of Ni, Fe, Bi, I and O elements in the composites. All the obtained binding energies were referenced to the C 1s (284.82 eV). In Fig. 2b, the two peaks at 854.16 eV and 873.62 eV were corresponding to the banding energies of Ni $2p_{3/2}$ and Ni $2p_{1/2}$ respectively, which suggests the typical banding energy of Ni^{2+}.[29] In Fig. 2c, the peak at 710.41 eV is corresponding to the binding energy of Fe $2p_{3/2}$, and the other peak at 724.72 eV is corresponding to Fe $2p_{1/2}$ signal. It indicates that the Fe element exists in the form of Fe^{3+} ion.[30] In Fig. 2d, the two strong peaks at 158.72 and 164.07 eV are assigned to Bi $4f_{7/2}$ and Bi $4f_{5/2}$ peaks of Bi^{3+} in the NFO/BOI nanocomposites with a peak difference of 5.35 eV. In Fig. 2e, we can observe two strong peaks at 618.71 and 630.22 eV, corresponding to I $3d_{5/2}$ and I $3d_{3/2}$ respectively. In addition, the peaks at 529.68 eV and 532.82 eV in Fig. 2f were attributed to O 1s. These two peaks indicate the different types of oxygen molecule such as lattice oxygen and surface oxygen. The XPS result further confirmed the formation of 15-NFO/BOI nanocomposites and intimate integration has been achieved, which agrees well with the XRD results.

3.3. SEM and TEM analysis

The surface morphologies and nanostructures of pure $NiFe_2O_4$, BiOI and 15-NFO/BOI nanocomposites were observed by FE-SEM. Fig. 3a displays the pure $NiFe_2O_4$ nanoparticles with grain sizes of 30–80 nm. It is observed that the $NiFe_2O_4$ nanoparticles appears a little aggregated together to some extent. From Fig. 3b, as-prepared pure BiOI is composed of cauliflower-like nanosheets with a range of diameter about 50–200 nm and an average thickness about 45 nm Fig. 3c demonstrated that $NiFe_2O_4$ nanoparticles adhered to the BiOI nanosheet in the 15-NFO/BOI nanocomposites, which would promote the

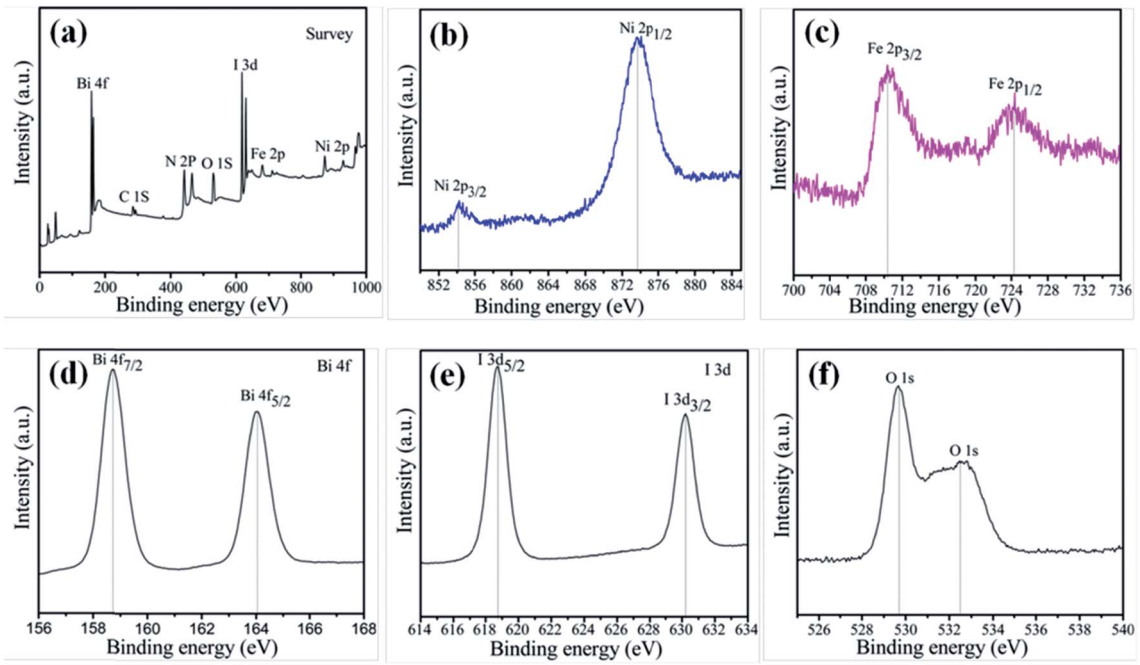

Fig. 2 XPS patterns of 15-NFO/BOI nanocomposites (a) survey; (b) Ni 2p; (c) Fe 2p; (d) Bi 4f; (e) I 3d; and (f) O 1s.

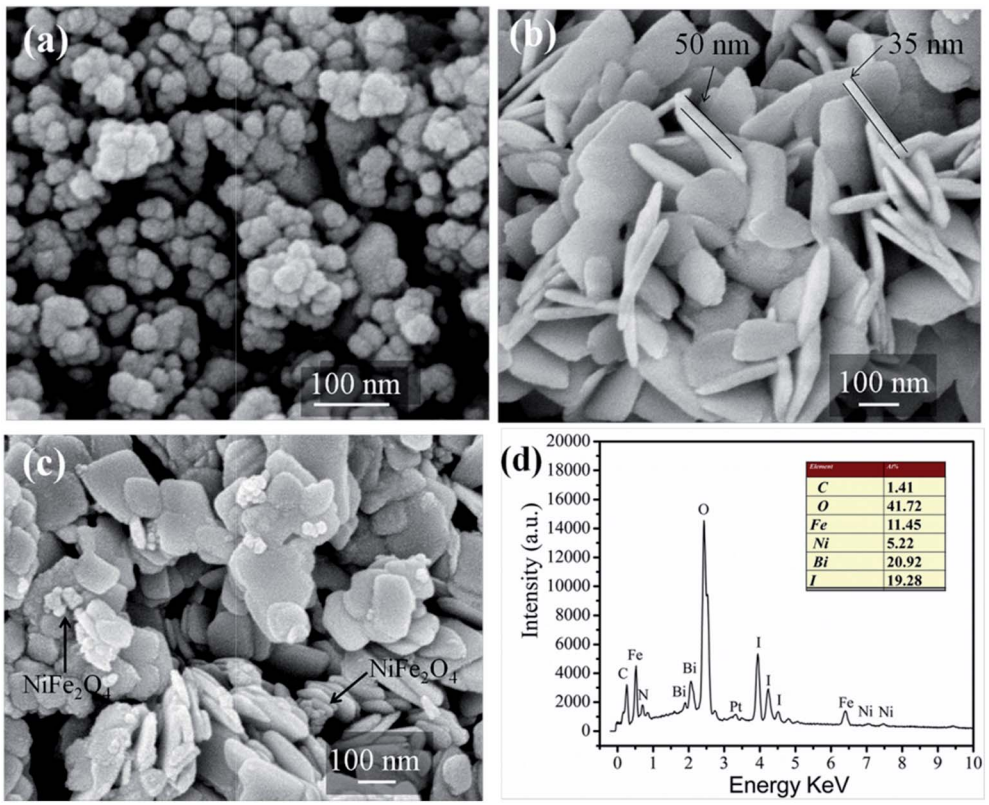

Fig. 3 SEM images of $NiFe_2O_4$ (a), BiOI (b) and 15-NFO/BOI nanocomposites (c) and EDS results of 15-NFO/BOI nanocomposites (d).

separation efficiency of photoinduced carriers. Furthermore, the result of EDS analysis (Fig. 3d) is in accord with the elements of 15-NFO/BOI nanocomposites. The elements Fe, Ni, Bi, I and O are present in 15-NFO/BOI composites, and the atomic ratio is the same as that of stoichiometric composition of the sample.

Fig. 4a shows the TEM image of NFO/BiOI nanocomposites, which are uniformly dispersed onto the BiOI without any accumulation. Moreover, in the HRTEM image of NFO/BiOI nanocomposites (Fig. 4c and d), the lattice fringes with a *d*-spacing of 0.286 nm and 0.295 nm from different regions could be corresponding to the (311) lattice planes of BiOI and (220) lattice planes of $NiFe_2O_4$, respectively. In addition, the elemental mappings are shown in Fig. 4e–j. It can be seen that the signals of Fe, Ni, Bi, I and O elements are the same in the spatial distribution.

3.4. Optical properties analysis

As we known, photocatalytic activity of semiconducting photocatalysts is closely related to the optical absorption ability and the optical properties play a vital role in determining the photocatalytic performance. Thus, UV-vis DRS was used to show the photoabsorption ability of the prepared samples and the results are displayed in Fig. 5a. It was found that BiOI showed a weak absorption in the range of wavelength around 580 nm. However, with the increase of $NiFe_2O_4$ (from 5 wt% to 20 wt%), the ability of NFO/BOI nanocomposites for absorption in the visible range became considerably stronger and exhibited a blue shift in the visible-light region compared with pure BiOI. The enhanced light absorption may accelerate the production of electron–hole pairs, thus improve the photocatalytic performance. Fig. 5b shows the band gap energy (E_g) of the pure $NiFe_2O_4$, BiOI and 15-NFO/BOI nanocomposites, they were calculated by the following formula based on the UV-vis DRS results:[31]

$$\alpha h\nu = A(h\nu - E_g)^{n/2} \quad (1)$$

where α, h, ν, n and A are absorption coefficient, plank constant, light frequency, the nature of transition and a constant respectively.[32,33] The value of n depended on the types of photon transition in semiconductors ($n = 1$ for direct transition and $n = 4$ for indirect transition). Sine $NiFe_2O_4$ and BiOI were the indirect transition and direct transition, respectively,[34] both substituted in eqn (1). Thus, E_g value of the samples can be estimated from a plot $(\alpha h\nu)^{n/2}$ *versus* photon energy ($h\nu$). The intercept of the tangent to *X* axis would give an approximation of the band gap energy of the sample. The band gap energy of pure $NiFe_2O_4$, BiOI were about 1.68 eV and 1.92 eV respectively, which agreed with the results previously reported.[35,36] When $NiFe_2O_4$ was introduced to BiOI, it created the impurity in the energy level of BiOI and hence modified the optical properties in visible region. Therefore, the 15-NFO/BOI ($E_g = 1.84$ eV) nanocomposites showed lower band gap values than pure BiOI.

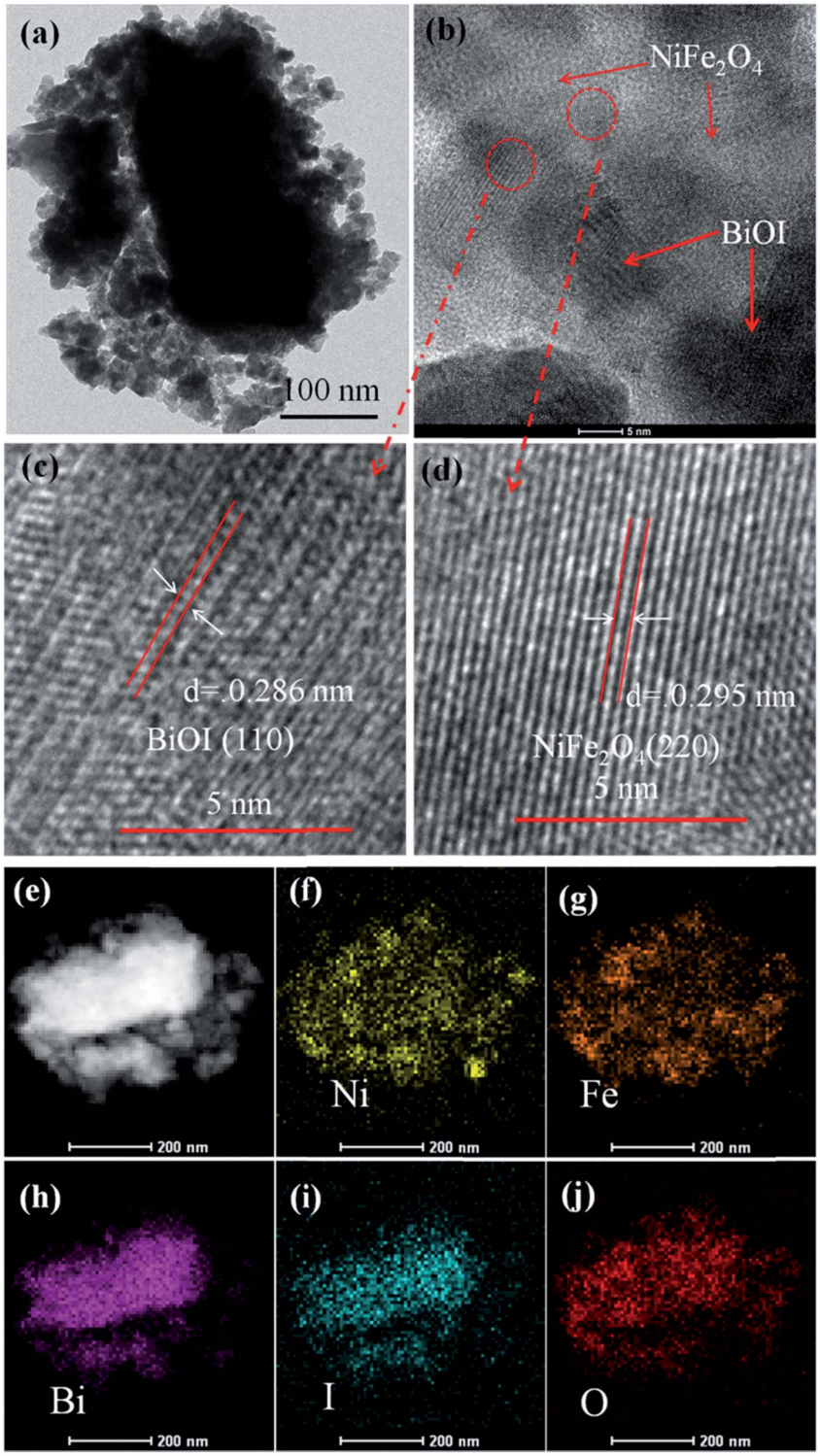

Fig. 4 TEM image (a), HRTEM image (b–d) and the corresponding elemental mapping images (e–j) of 15-NFO/BOI nanocomposites.

3.5. Magnetic hysteresis loops analysis

The magnetic hysteresis loops of the 15-NFO/BOI and pure $NiFe_2O_4$ under an applied magnetic field of ±2 T at room temperature were shown in Fig. 6. The pure $NiFe_2O_4$ nanoparticles exhibited a typical ferromagnetic behavior, and its saturation magnetization (M_s) is about 38.54 emu g^{-1}. The M_s of 15-NFO/BOI nanocomposites was about 25.35 emu g^{-1}, which still had higher M_s compared with other magnetic photocatalyst reported earlier.[37] The ferromagnetic property of as-synthesized 15-NFO/BOI catalysts ensures the convenient magnetic separation after used. As shown in the inset of Fig. 6, the 15-NFO/BOI

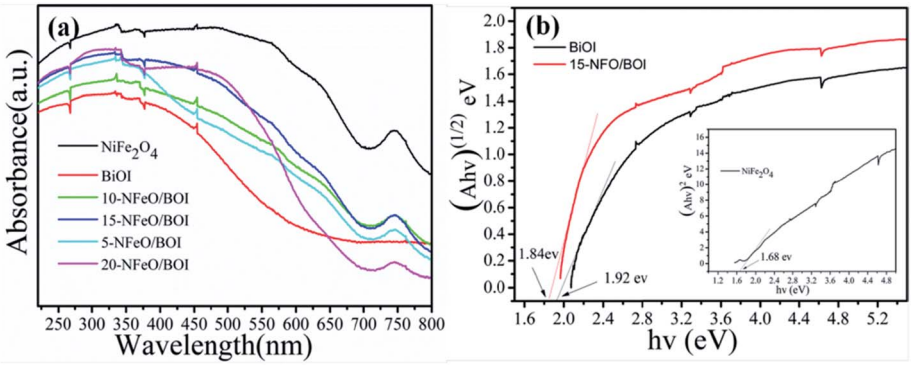

Fig. 5 (a) UV-vis diffuse reflectance spectra (DRS) of as-prepared samples, (b) band gap energies of BiOI, 15-NFO/BOI and $NiFe_2O_4$.

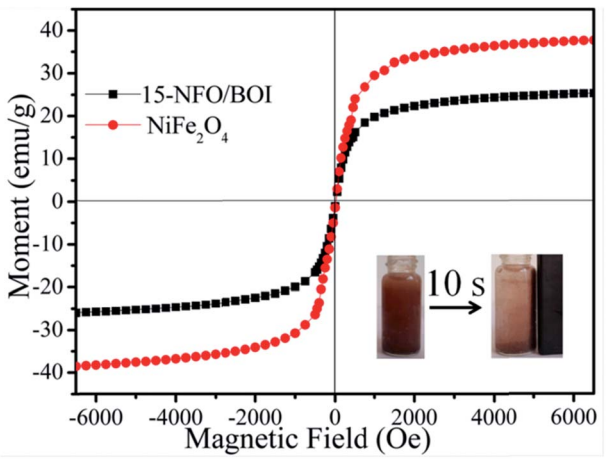

Fig. 6 Magnetic hysteresis loops of 15-NFO/BOI nanocomposites and $NiFe_2O_4$ (inset: the magnetic separation of 15-NFO/BOI nanocomposites by a magnet).

nanocomposites could be easily separated from the wastewater with a common magnet and quickly collected on the side of the glass vial for 10 s, which indicates that 15-NFO/BOI nanocomposites might be easily recycled from wastewater by external magnetic field.[38]

3.6. Photocatalytic activity

RhB is a typical artificial aromatic compound dye with a molecular formula $C_{28}H_{31}C_lN_2O_3$ and commonly used as a colour additive in industry although it is not easy to decompose, highly toxic and probably causes cancer.[39] The degradation of RhB was used here to evaluate the photocatalytic performance of the as-prepared all samples under visible-light irradiation at room temperature, as shown in Fig. 7a. Obviously, the pure $NiFe_2O_4$ and BiOI possessed poor photocatalytic ability, which are consistent with the reported values.[40,41] The photocatalytic activities of the NFO/BOI nanocomposites increased firstly and then decreased with the increase of $NiFe_2O_4$ content from 5% to 20%. Among all proportions 15-NFO/BOI showed the best photocatalytic efficiency of approximately 91.6% under visible-light irradiation for 120 min. It is clearly evident that the weight percent of $NiFe_2O_4$ has a substantial influence on the degradation RhB reaction and could improve the photocatalytic activity. Moreover, the degradation of RhB was used to evaluate the photocatalytic performance of the 15-NFO/BOI physically mixed under the same condition. It was found that photocatalytic activity was nearly the same as that of $NiFe_2O_4$. UV-vis spectra were severally observed during degradation of RhB solution under visible-light irradiation. Fig. 7b shows that the intensity of the characteristic absorption peaks of RhB catalyzed by 15-NFO/BOI nanocomposites. It decreased as reaction time went on and molecules of RhB were almost completely degraded after the light irradiation for 120 min. The results disclosed that the 15-NFO/BOI nanocomposites possessed a powerful photo-oxidizing ability and could be utilized as a photocatalyst for practical applications.

To reveals the reaction kinetics of the photo-degradation of RhB on different photocatalysts, the degradation rates were computed using the following pseudo-first-order kinetics (eqn (2))

$$\ln(C_0/C_t) = K_{app}t \quad (2)$$

where C_0, C_t, and K_{app} stand for the initial concentration, the concentration at time t, and the apparent pseudo-first-order rate constant respectively.[42,43] As shown in Fig. 7c, $-\ln(C_t/C_0)$ exhibits a well linear relationship with irradiation time and the photocatalytic reaction belongs to the pseudo-first-order reaction. The K_{app} value of the RhB solution decomposition obtained for BiOI, $NiFe_2O_4$, 5-NFO/BOI, 10-NFO/BOI, 15-NFO/BOI and 20-NFO/BOI are 3.18×10^{-3}, 4.6×10^{-3}, 7.28×10^{-3}, 8.725×10^{-3}, 1.64×10^{-2} and 1.225×10^{-2} min^{-1} respectively. Among these composites, the 15-NFO/BOI nanocomposites displayed the maximum degradation rate constant, which was superior to the as-prepared other samples.

For the purpose of testing the recyclability and stability of the 15-NFO/BOI photocatalysts, multiple cycle degradation experiments were carried out. The experiments were performed under the identical condition. After the completion of each experiment, the photocatalyst could be quickly collected by an external magnet from the dye solution, washed, dried, and then applied in the next run. As shown in Fig. 7d, their catalytic

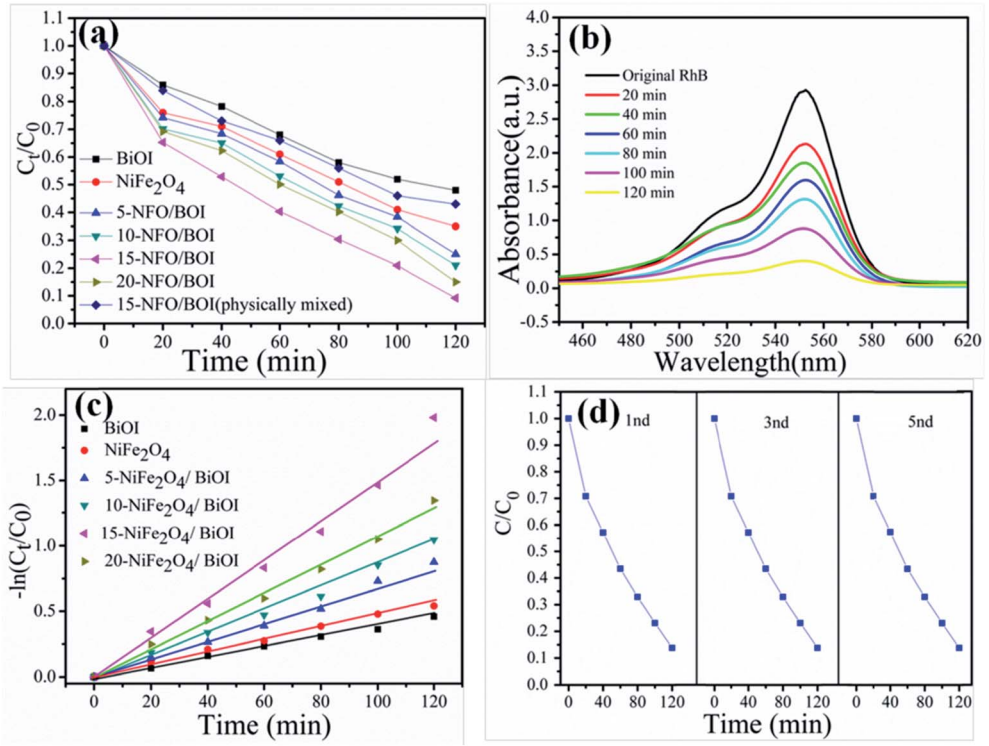

Fig. 7 (a) Photocatalytic degradation of RhB for all samples under visible-light irradiation; (b) absorption spectra of RhB over 15-NFO/BOI nanocomposites; (c) $-\ln(C_t/C_0)$ *vs.* time plot for photodegradation of RhB by different catalysts; (d) cycling degradation rate for RhB of 15-NFO/BOI nanocomposites under visible-light irradiation.

activity shows no notable decrease even after the fifth recycle. Consequently, the as-synthesized 15-NFO/BOI nanocomposites can work as effective photocatalysts for dye degradation with good stability.

Furthermore, the phase and morphology changes of the 15-NFO/BOI nanocomposites were characterized after cycling light irradiation. The 15-NFO/BOI nanocomposites was examined by XRD and no detectable difference was observed between the as-prepared and the used samples (Fig. 8a). Hence, the 15-NFO/BOI nanocomposites had excellent photostability. SEM images in Fig. 8(b and c) show the 15-NFO/BOI nanocomposites before and after the photocatalytic degradation reaction. Fig. 8b shows the morphology of the catalyst before the photocatalytic reaction, in which distinct $NiFe_2O_4$ aggregates were attached to the edge and surface of the BiOI sample. After the photocatalytic degradation reaction, as shown in Fig. 8c, the surface structure and morphology of the 15-NFO/BOI nanocomposites remained intact, further indicating the structural stability of the 15-NFO/BOI sample.

In order to investigate whether the 15-NFO/BOI nanocomposites are of wide applications or not, they have been further tested the photocatalytic performance of CV and MB under the same conditions. Fig. 9a and c show the photocatalytic performances of the as-prepared all samples. The 15-NFO/BOI nanocomposites exhibited the best photocatalytic ability for CV and MB removal. Furthermore, about 92.5% CV and 96% MB were degraded within 120 min, respectively. UV-vis spectra were severally observed during degradation of CV solution and MB solution under visible-light irradiation, respectively, as shown in Fig. 9b and d. The decomposed behaviours of CV solution and MB solution over the photocatalyst of 15-NFO/BOI nanocomposites. It was obvious that the

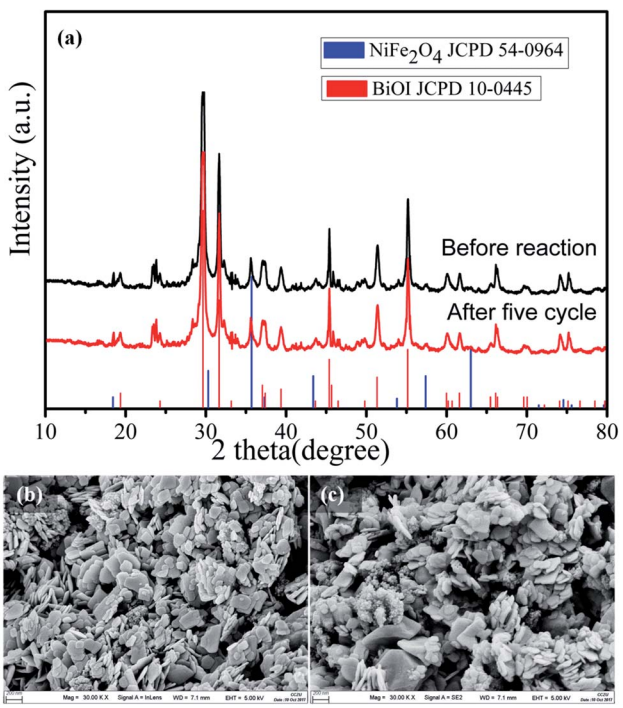

Fig. 8 (a) XRD patterns, (b) and (c) SEM images before reaction and after five cycle of 15-NFO/BOI nanocomposites.

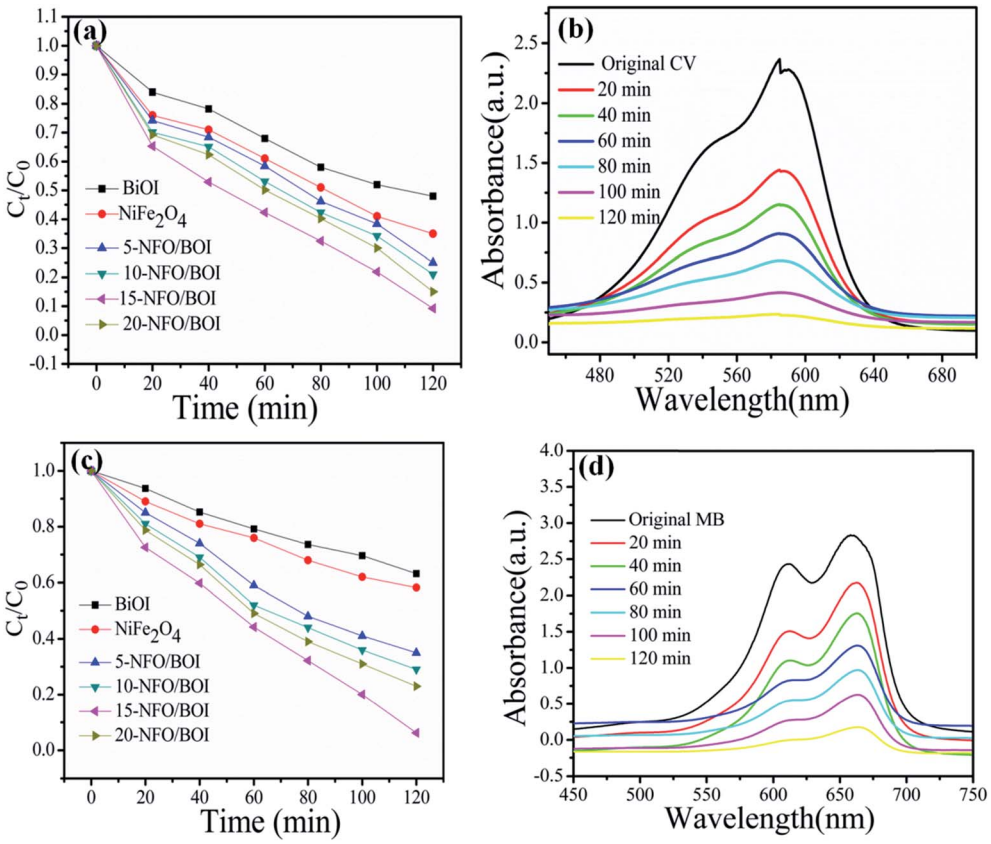

Fig. 9 (a) Photocatalytic degradation and (b) absorption spectra of CV by 15-NFO/BOI nanocomposites photocatalysts under visible-light irradiation; (c) photocatalytic degradation and (d) absorption spectra of MB by 15-NFO/BOI nanocomposites photocatalysts under visible-light irradiation.

peak intensity of the characteristic absorption at about 585 nm and 658 nm were found to be decreased as reaction time went on, respectively. The results indicate that the 15-NFO/BOI nanocomposites was efficient in catalyzing degradation of dyes under visible-light irradiation.

3.7. Photocatalytic mechanism discussion

In order to better reveal the photocatalytic mechanism, we carried out the trapping experiments, iso-propyl alcohol (IPA), disodium ethylene-diaminetetraacetate (EDTA-2Na) and benzoquinone (BQ) were used as the scavengers of the hydroxyl radical ($^{\bullet}OH$), holes and superoxide radical ($^{\bullet}O_2^{\bullet-}$), respectively. As shown in Fig. 10, addition of IPA had almost no effect on RhB degradation for NFO/BOI nanocomposites, indicating that no $^{\bullet}OH$ radicals were generated. Nevertheless, a significant decrease was observed after the addition of BQ and EDTA-2Na, demonstrating that $^{\bullet}O_2^{\bullet-}$ and holes were involved in the RhB decomposition process.

In order to investigate the migration and separation efficiencies of photo-generated charge carriers in pure BiOI and 15-NFO/BOI nanocomposites, a room-temperature PL emission spectrum were measured, as shown in Fig. 11. For pure BiOI a strong emission peak at 607 nm were observed. The similar PL spectra was obtained for 15-NFO/BOI nanocomposites. It could be seen that the peak intensity of the spectrum for the 15-NFO/BOI nanocomposites is lower than that of the pure BiOI sample. As we known, intensity of the PL spectrum of a semiconductor mainly results from the recombination of electrons–holes pairs. Hence, there is a strong correlation between PL emission

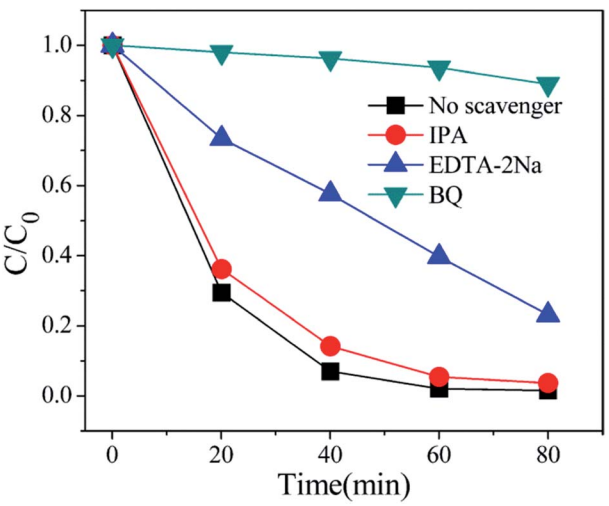

Fig. 10 Reactive species trapping experiments over 15-NFO/BOI nanocomposites.

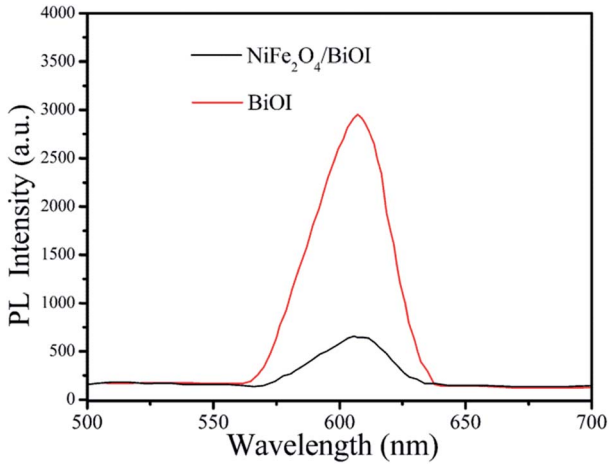

Fig. 11 PL spectra (excited at 325 nm) of pure BiOI and 15-NFO/BOI nanocomposites.

intensity and separation of the photo-generated charge carriers. For this reason, the weakened emission intensity in 15-NFO/BOI nanocomposites indicates inhibition of electron–hole recombination due to the co-catalytic effect of $NiFe_2O_4$, which lengthens the lifetime of charge carriers and is beneficial for the improvement of photocatalytic activity.

Photocurrent measurements were performed to further investigate the generation and transfer of photoexcited charge carriers in the photocatalytic process. As shown in Fig. 12, 15-NFO/BOI nanocomposites exhibited enhanced photocurrent responses compared to the pure BiOI and $NiFe_2O_4$. These photocurrent efficiencies are consistent with the degrees of photocatalytic activity. Therefore, in the 15-NFO/BOI nanocomposites, the separation and transfer efficiency of the photoinduced electrons–holes pairs was improved by the interfacial interactions between $NiFe_2O_4$ and BiOI.

To describe mechanism of the enhanced photocatalytic activity of the NFO/BOI nanocomposites under visible-light irradiation, the corresponding conduction band (CB) and valence band (VB) positions for $NiFe_2O_4$ and BiOI were theoretically computed using the atom's Mulliken electronegativity definition (eqn (3) and (4)):

$$E_{VB} = \chi - E_c + 0.5E_g \quad (3)$$

$$E_{CB} = E_{VB} - E_g \quad (4)$$

where E_{VB} is the VB potential, E_{CB} is the CB potential, E_c is the energy of free electrons on the hydrogen scale (*ca.* 4.5 eV), E_g is the band gap energy and χ is the absolute electronegativity of the semiconductor.[44] Therefore, the E_{VB} and E_{CB} of BiOI were computed to be 2.64 eV and 0.718 eV, whereas the energies for $NiFe_2O_4$ were about 1.28 eV and −0.6 eV, respectively.

According to the above results, the possible photocatalytic mechanisms of the NFO/BOI nanocomposites were illustrated in Fig. 13. Under visible-light irradiation ($\lambda > 420$ nm), the electrons of BiOI and $NiFe_2O_4$ can be excited and then transit from the VB position to the position of CB. Then the electrons on the CB of $NiFe_2O_4$ jumped to inject into the more positive CB of the surrounding BiOI, while the same amount of holes in the VB of BiOI migrated to the more negative VB edge position of $NiFe_2O_4$, leading to the rapid separation of the photoinduced electrons and holes. Because of the CB potentials of BiOI (0.718 eV) are more positive than that of $O_2/{}^{\bullet}O_2^{\bullet-}$ (−0.33 eV *vs.* NHE),[45] the oxygen (O_2) in the solution was trapped by the electrons to form ${}^{\bullet}O_2^{\bullet-}$ on the NFO_4/BOI surface, then ${}^{\bullet}O_2^{\bullet-}$ further oxidized the organic contaminants to H_2O and CO_2 as final products. However, the photo-induced holes accumulated on $NiFe_2O_4$ cannot oxidize surface-bound water or hydroxyl group into ${}^{\bullet}OH$ (2.38 V *vs.* NHE),[46] due to the more negative VB potential of $NiFe_2O_4$, indicating that photogenerated holes of such catalyst have strong oxidation ability than ${}^{\bullet}OH$ and H_2O_2. Therefore, photogenerated holes react directly with adsorbed molecules of RhB to produce degradation products. As a result, both of the ${}^{\bullet}O_2^{\bullet-}$ and holes play important roles in degradation of organic pollutants.

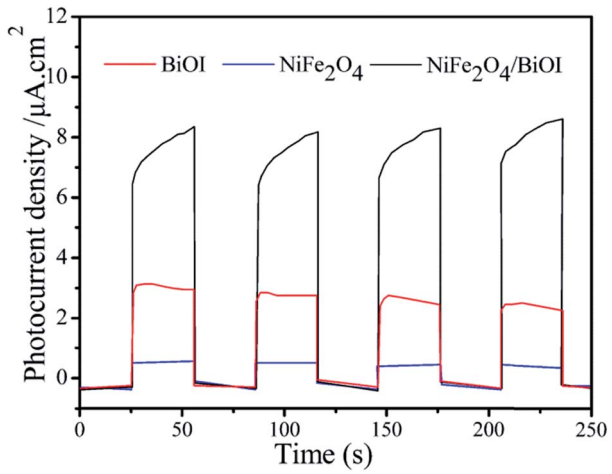

Fig. 12 Photocurrent responses of the samples under visible-light irradiation.

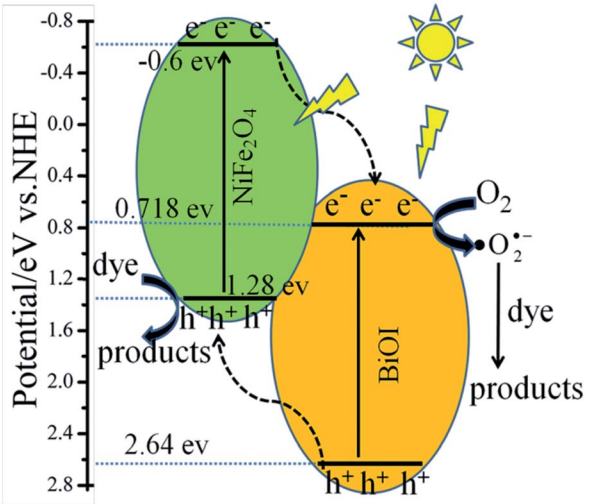

Fig. 13 Schematic illustration of excitation and separation of photo-induced electron–hole pairs for NFO_4/BOI nanocomposites under visible light irradiation.

4. Conclusions

In this work, novel multifunctional NFO/BOI nanocomposites were fabricated through the hybridization of $NiFe_2O_4$ and BiOI. For the heterogeneous materials, the optimal content was achieved to be the 15-NFO/BOI, which exhibited excellent capacity for the degradation of RhB, CV and MB under visible-light irradiation. The enhanced photodegradation performance can be attributed to the promoted separation and inhibited recombination of electron–holes pairs in the heterostructures of NFO/BOI nanocomposites. Moreover, the excellent room temperature ferromagnetism and stability of NFO/BOI nanocomposites ensure the convenient magnetic separation. Since the unique NFO/BOI material with high activity and recyclable magnetic separation, it have potential applications in organic pollutant removal and environmental remediation.

Conflicts of interest

The authors declare no competing financial interest.

Acknowledgements

This work was supported by the National Natural Science Foundation of China (61107055) and the Specialized Research Fund for the Doctoral Program of Jiangsu University of Technology (KYY17011).

References

1 C. W. Kim, S. P. Suh, M. J. Choi, Y. S. Kang and Y. S. Kang, *J. Mater. Chem. A*, 2013, **1**, 11820–11827.
2 J. J. Xu, Y. M. Hu, C. Zeng, Y. H. Zhang and H. W. Huang, *J. Colloid Interface Sci.*, 2017, **505**, 719–727.
3 J. Z. Y. Tan, N. M. Nursam, F. Xia, M. A. Sani, W. Li, X. D. Wang and R. A. Caruso, *ACS Appl. Mater. Interfaces*, 2017, **9**, 4540–4547.
4 W. Subramonian, T. Y. Wu and S. P. Chai, *J. Environ. Manage.*, 2017, **187**, 298–310.
5 F. Chen, D. Li, B. Luo, M. Chen and W. Shi, *J. Alloys Compd.*, 2017, **694**, 193–200.
6 W. Li, D. H. Chen, F. Xia, J. Z. Y. Tan, P. P Huang, W. G. Song, N. M. Nursam and R. A. Caruso, *Environ. Sci.: Nano*, 2016, **3**, 94–106.
7 J. Wen, J. Xie, X. Chen and X. Li, *Appl. Surf. Sci.*, 2017, **391**, 72–123.
8 A. I. Borhan, P. Samoila, V. Hulea, A. R. Iordan and M. N. Palamaru, *J. Taiwan Inst. Chem. Eng.*, 2014, **45**, 1655–1660.
9 Y. Bu and Z. Chen, *Electrochim. Acta*, 2014, **144**, 42–49.
10 I. K. Konstantinou and T. A. Albanis, *Appl. Catal., B*, 2004, **49**, 1–14.
11 X. Chen and S. S. Mao, *Chem. Rev.*, 2007, **107**, 2891–2959.
12 F. Niu, L. S Zhang, C. Q. Chen, W. Li, L. Li, W. G. Song and L. Jiang, *Nanoscale*, 2010, **2**, 1480–1484.
13 Z. M. He, Y. M. Xia, B. Tang, X. F. Jiang and J. B. Su, *Mater. Lett.*, 2016, **184**, 148–151.
14 K. Ji, H. Dai, J. Deng, H. Zang, H. Arandiyan, S. Xie and H. Yang, *Appl. Catal., B*, 2015, **168–169**, 274–282.
15 W. Cui, W. An, L. Liu, J. Hu and Y. Liang, *J. Hazard. Mater.*, 2014, **280**, 417–427.
16 H. Huang, X. Han, X. Li, S. Wang, P. K. Chu and Y. Zhang, *ACS Appl. Mater. Interfaces*, 2015, **7**, 482–492.
17 F. Chen, C. Niu, Q. Yang, X. Li and G. Zeng, *Ceram. Int.*, 2016, **42**, 2515–2525.
18 Y. Yu, C. Y. Cao, H. Liu, P. Li, F. F Wei, Y. Jiang and W. G. Song, *J. Mater. Chem. A*, 2014, **2**, 1677–1681.
19 X. Li, C. Niu, D. Huang, X. Wang, X. Zhang, G. Zeng and Q. Niu, *Appl. Surf. Sci.*, 2013, **286**, 40–46.
20 X. Zhang, L. Zhang, T. Xie and D. Wang, *J. Phys. Chem. C*, 2009, **113**, 7371–7378.
21 S. Balaji, R. K. Selvan, L. J. Berchmans, S. Angappan, K. Subramanian and C. O. Augustin, *Mater. Sci. Eng., B*, 2005, **119**, 119–124.
22 S. Gautam, P. Shandilya, V. P. Sing, P. Raizada and P. Singh, *Journal of Water Process Engineering*, 2016, **14**, 86–100.
23 P. Chen, X. Xing, H. F. Xie, Q. Sheng and H. X. Qu, *Chem. Phys. Lett.*, 2016, **660**, 176–181.
24 C. T. Cherian, J. Sundaramurthy, M. V. Reddy, P. S. Kumar, K. Mani, D. Pliszka, C. H. Sow, S. Ramakrishna and B. V. R. Chowdari, *ACS Appl. Mater. Interfaces*, 2013, **5**, 9957–9963.
25 H. Song, L. P. Zhu, Y. G. Li, Z. R. Lou, M. Xiao and Z. Z. Ye, *J. Mater. Chem. A*, 2015, **3**, 8353–8360.
26 T. H. Yu, W. Y. Cheng, K. J. Chao and S. Y. Lu, *Nanoscale*, 2013, **5**, 7356–7360.
27 M. Dhiman, A. Goyal, V. Kumar and S. Singhal, *New J. Chem.*, 2016, **40**, 10418–10431.
28 J. Henle, P. Simon, A. Frenzel, S. Scholz and S. Kaskel, *Chem. Mater.*, 2007, **19**, 366–373.
29 H. Y. Ji, X. C. Jing, Y. G. Xu, J. Yan, H. P. Li, Y. P. Li, L. Y. Huang, Q. Zhang, H. Xu and H. M. Li, *RSC Adv.*, 2015, **5**, 57960–57967.
30 H. S. Kim, D. J. Kim, B. S. Kwak, G. B. Han, M. H. Um and M. Kang, *Chem. Eng. J.*, 2014, **243**, 272–279.
31 A. Murphy, *Sol. Energy Mater. Sol. Cells*, 2007, **91**, 1326–1337.
32 Y. Ohko, K. Hashimoto and A. Fujishima, *J. Phys. Chem. A*, 1997, **101**, 8057–8062.
33 N. M. Nursam, J. Z. Y. Tan, X. D. Wang, W. Li and F. Xia, *ChemistrySelect*, 2016, **1**, 4868–4878.
34 Z. H. Shah, Y. z. Ge, W. Y. Ye, X. J. Lin, S. F. Zhang and R. W. Lu, *Mater. Chem. Phys.*, 2017, **198**, 73–82.
35 X. w. Li, L. Wang, L. Zhang and S. p. Zhuo, *Appl. Surf. Sci.*, 2017, **419**, 586–594.
36 Y. W. Zhou, S. S. Fang, M. Zhou, G. Q. Wang, S. Xue, Z. Y. Li, S. Xu and C. Yao, *J. Alloys Compd.*, 2017, **696**, 353–361.
37 H. S. Kim, D. J. Kim, B. S. Kwak, G. B. Han, M. H. Um and M. Kang, *J. Chem. Eng.*, 2014, **243**(27), 2–9.
38 D. D. Lv, D. F. Zhang, X. Y. Liu, Z. R. Liu, L. J. Hu, X. P. Pu, H. Y. Ma, D. C. Li and J. M. Dou, *Sep. Purif. Technol.*, 2016, **158**, 302–307.
39 J. T. Deng, L. Liu, T. J. Niu and X. S. Sun, *Appl. Surf. Sci.*, 2017, **403**, 531–539.

40 Z. M. He, Y. M. Xia, B. Tang and J. B. Su, *Mater. Res. Express*, 2017, **4**, 095501–095508.
41 Y. Guan, H. Qian, J. Q. Guo, S. G. Yang, X. Wang, S. M. Wang and Y. S. Fu, *Appl. Clay Sci.*, 2015, **114**, 124–132.
42 Y. Q. Wang, X. F. Cheng, X. T. Meng, H. W. Feng, S. G. Yang and C. Sun, *J. Alloys Compd.*, 2015, **632**, 445–449.
43 L. Zhang, X. Zhang, Y. Q. Huang, C. L. Pan, J. S. Hu and C. M. Hou, *RSC Adv.*, 2015, **5**, 30239–30247.
44 L. Cao, D. H. Chen, W. Li and R. A. Caruso, *ACS Appl. Mater. Interfaces*, 2014, **6**, 13129–13137.
45 J. Kim, C. W. Lee and W. Choi, *Environ. Sci. Technol.*, 2010, **44**, 6849–6854.
46 W. Li, C. Y. Cao, L. Y. Wu, M. F. Ge and W. G. Song, *J. Hazard. Mater.*, 2011, **198**, 143–150.